Submitted

D. J. Arnold, Y. M. Stokes, and J. E. F. Green
Thin-film flow in helically-wound rectangular channels of arbitrary torsion and curvature
Journal of Fluid Mechanics, 2014; 764:76-94

Thin-film flow in helically-wound rectangular channels of arbitrary torsion and curvature

D. J. Arnold[1], Y. M. Stokes[1]†, J. E. F. Green[1]

[1]School of Mathematical Sciences, The University of Adelaide, Adelaide, SA 5005, Australia

(Received ?; revised ?; accepted ?. - To be entered by editorial office)

Laminar helically-symmetric gravity-driven thin-film flow down a helically-wound channel of rectangular cross-section is considered. We extend the work of Stokes *et al.* (2013) and Lee *et al.* (2014) to channels with arbitrary curvature and torsion or, equivalently, arbitrary curvature and slope. We use a non-orthogonal coordinate system and, remarkably, find an exact steady-state solution. We find that the free-surface shape and flow have a complicated dependence on the curvature, slope and flux down the channel. Moderate to large channel slope has a significant effect on the flow in the region of the channel near the inside wall, particularly when the curvature of the channel is large. This work has application to flow in static spiral particle separators used in mineral processing.

1. Introduction

In this paper we study the gravity-driven flow of a viscous fluid in a channel of rectangular cross-section, helically wound about a vertical axis as shown in figure 1, where the fluid depth is assumed to be small. The channel is oriented such that the bottom is horizontal in the radial direction. We neglect the entrance and exit regions and assume that the flow is helically symmetric; that is, independent of distance along any helix of the same pitch and orientation as the channel centreline. Thus the flow, which comprises a primary flow down the channel and a secondary flow in the cross-sectional plane, depends only on position in the two-dimensional cross-section. We make no assumptions of small channel torsion or slope and so extend the work of Stokes *et al.* (2013) for channels of small centreline torsion, and of Lee *et al.* (2014) for channels of small centreline slope. Using a non-orthogonal coordinate system, as in Lee *et al.* (2014), we are, remarkably, able to find an exact solution of our thin-film model. Our use of a nonorthogonal coordinate system and accounting for a channel slope that varies with position across the channel width reveal corrections to the results of Stokes *et al.* (2013).

The study of flows in curved geometries has been motivated by flows in rivers and pipes (Thomson 1876, 1877; Dean 1927, 1928), the circulatory system (Lynch *et al.* 1996; Siggers & Waters 2005, 2008), and the cochlea (Manoussaki & Chadwick 2000). The impact of Dean's work was such that these flows are often termed "Dean flow".

An application of particular interest to the authors, and which has attracted considerable attention over several decades since the work of Holland-Batt (1975, 1989), is the separation of minerals or coal from crushed ore in static spiral separators. These consist of a helically-wound channel, down which a slurry of crushed ore and water is poured. The resulting fluid motion serves to sort the particles across the width of the channel by size/density, and simple sectioning of the flow at the bottom of the channel allows particles of different sizes/densities to be collected separately. Whilst such devices are commonly used, their design is hampered by a lack of quantitative understanding of the

† Email address for correspondence: yvonne.stokes@adelaide.edu.au

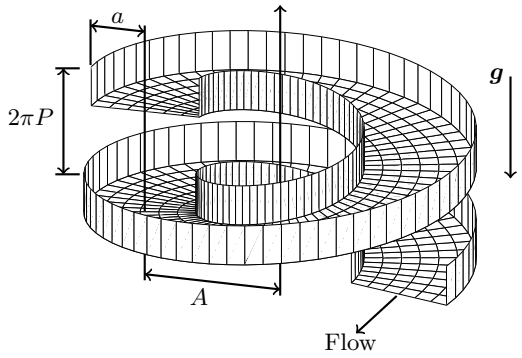

Figure 1: A helically-wound rectangular channel of width $2a$. The centreline is a helix of radius A and pitch $2\pi P$.

fluid and particle motion, so that experimentation and empirical formulae are heavily used during design; for a summary of the design process see Holland-Batt (1995). A desire for a better quantitative understanding to aid design has driven experimental, theoretical and computational research on both clear fluid and particle laden flow in helically-wound channels. A steady-state empirical model of particle-free flow in a rectangular channel was developed by Holland-Batt (1989), in which the primary flow down the channel is described by a Manning law in an inner region near the central column around which the channel is wound, and a free vortex in the outer region. Experimental work followed to attempt to validate this model (Holtham 1990; Holland-Batt & Holtham 1991; Holtham 1992) but the small fluid depth typical of spiral separators makes measuring flow velocity and free-surface shape very difficult. While this work did confirm the existence of the predicted secondary flow, show the flow to be laminar in much of the flow domain, and indicate that the flow had reached a fully-developed profile within two spiral turns, (justifying the assumption of helical symmetry) it gave only crude estimates of flow velocities with errors as high as $\pm 30\%$, precluding meaningful quantitative comparison of experiments with models. Recently Holland-Batt (2009) adapted the model for large-diameter rectangular spiral channels, with the strength of the free vortex primary flow computed using laminar, Manning and Bagnold shear equations; little difference was found in the velocity profiles between the three options. Computational simulations were performed by Wang & Andrews (1994), Matthews *et al.* (1998, 1999) and Stokes (2001). Das *et al.* (2007) used the semi-empirical model of Holland-Batt (1989) to investigate the behaviour of particles in such a flow, assuming that the particles do not modify the flow, while acknowledging that this model sometimes predicts larger flow depths than reported in experiments.

Flows in spiral separators are typically quite shallow. In experiments performed by Holtham (1992) using two commercially-available spiral separators with an approximate width of 280mm, the fluid depth was 1–12mm, an aspect ratio $\delta < 0.1$. Thus, Stokes *et al.* (2004, 2013) and Lee *et al.* (2014) have exploited the small depth of the flow to develop thin-film models of particle-free and particle-laden flow in helically-wound channels. These studies have considered limiting cases of channel geometry, such as small curvature, torsion or slope and indicate that the assumption made by Holland-Batt (1989, 2009) of a free-vortex primary flow in the channel is not, in general, valid in these limits. In this paper we retain the assumption of small fluid depth but consider particle-free

flow in channels of arbitrary curvature and torsion. In future work, the model will be extended using the approach of Lee *et al.* (2014) to investigate particle-laden flow.

In the study of flows in curved geometries, considerable attention has been given to the choice of coordinate system. The natural s, r, θ (or s, x, y) coordinate system, where s is arclength along the axis of the pipe or channel and r, θ (x, y) are polar (Cartesian) coordinates in the cross-section, is non-orthogonal, with non-zero off-diagonal elements in the metric tensor. To avoid the complexity of dealing with non-orthogonal coordinates, Germano (1982, 1989) obtained an orthogonal coordinate system by rotating the $\theta = 0$ line with position s. Zabielski & Mestel (1998) pointed out that, except in the zero-torsion limit, this coordinate system does not allow true helical symmetry (quantities are independent of distance s, while true helical symmetry requires that quantities not change along any helical path with the same pitch as the channel centreline) and proposed an alternative coordinate system which does allow true helical symmetry. Unlike the problems considered by these authors, the flows of interest here have a free-surface, for which neither of these coordinate systems are easy to use. Hence we adopt the more intuitive non-orthogonal coordinate system previously employed by Manoussaki & Chadwick (2000) for the study of inviscid fluid flow in the cochlea (modelled as a rectangular duct), and which is similar to the natural (s, x, y) system.

The structure of this paper is as follows. In section 2 we describe the coordinate system and the mathematical model, and then solve the model exactly. Results are presented and discussed in section 3 and our summary and conclusions are given in section 4.

2. Mathematical model

We consider steady, helically symmetric flow of an incompressible viscous fluid down a channel of constant rectangular cross-section with width $2a$, the centreline of which is a helix of pitch $2\pi P$ and radius A, as shown in figure 1. The channel is aligned so that its bottom is horizontal is the radial direction.

2.1. *Non-orthogonal coordinates*

Following Manoussaki & Chadwick (2000) and Lee *et al.* (2014), we employ a helical coordinate system in which a point $\boldsymbol{x}$ is specified using three variables, (r, β, z), as follows

$$\boldsymbol{x}(r, \beta, z) = r\cos\beta\,\boldsymbol{i} + r\sin\beta\,\boldsymbol{j} + (P\beta + z)\,\boldsymbol{k}. \tag{2.1}$$

Here r is the radial distance from the axis of the helix, β is an angle from a reference direction, and z is the vertical distance above the bottom surface of the channel. Using this description, the assumption of helical symmetry implies that the flow is independent of the angle β. The free-surface profile is given as $S(r, z) = h_z(r) - z = 0$, where $h_z(r)$ is the fluid depth in the vertical direction at radial position r.

The basis vectors in this coordinate system, $\boldsymbol{e}_r$, $\boldsymbol{e}_\beta$ and $\boldsymbol{e}_z$, are non-orthogonal and hence tensor calculus is required to determine differential operators. Once helical symmetry has been enforced by assuming derivatives with respect to β vanish, a new coordinate direction, n, is introduced to replace z. The new coordinate is in the direction of unit vector $\boldsymbol{e}_n = \boldsymbol{e}_r \times \boldsymbol{e}_\beta$, orthogonal to $\boldsymbol{e}_r$ and $\boldsymbol{e}_\beta$, so the direction $\boldsymbol{e}_n$ varies with position across the channel. Figure 2 shows the coordinate system on the channel centreline and in a vertically-cut cross-section of the channel. The normal direction is more intuitive, particularly for very steep channels, when the axial and vertical directions can nearly coincide. Velocity components in the r, β and n directions are v^r, v^β and v^n, respectively, and the free-surface profile is given by $S_n(r, n) = h_n(r) - n = 0$. The helically-symmetric

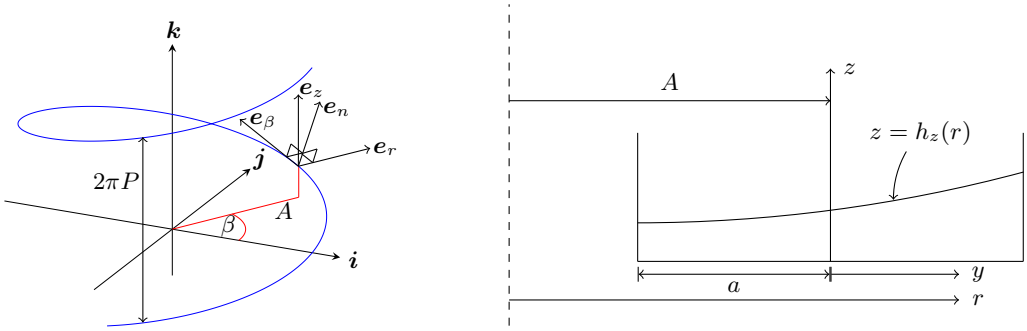

Figure 2: The coordinate system (a) on the helical centreline of radius A and pitch $2\pi P$, and (b) in a vertically-cut cross-section of the channel.

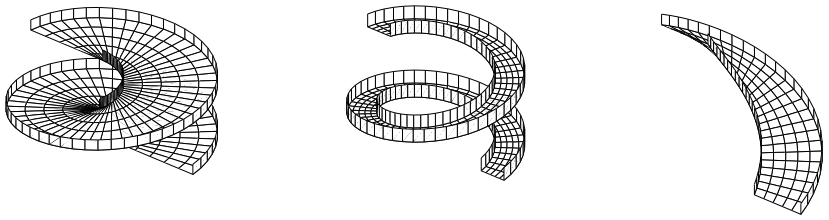

(a) $\epsilon = 0.8$, $\lambda = 1$ (b) $\epsilon = 0.2$, $\lambda = 1$ (c) $\epsilon = 0.5$, $\lambda = 5$

Figure 3: Channels with (a) large curvature and moderate slope, (b) small curvature and moderate slope, (c) large slope and moderate curvature. Note each channel is the same width, but the images are not shown at the same scale, in order to preserve detail.

Navier-Stokes equations in the r, β, n coordinate system are given in appendix A; see Lee *et al.* (2014) for details of the derivation.

2.2. *Thin-film equations*

Since the fluid depth is assumed to be small relative to the channel half-width a, we employ a thin-film approximation to simplify the Navier-Stokes equations. Specifically, if $\bar{h}$ is a representative fluid depth in the direction normal to the channel bottom (*i.e.*, the $\boldsymbol{e}_n$ direction), then $\delta = \bar{h}/a$ is a measure of the aspect ratio of the flow domain, and we assume that $\delta \ll 1$. We will define δ in terms of the physical parameters of the problem in section 2.4.

Next, we nondimensionalise our governing equations using the channel half-width, a, axial velocity scale, U (to be specified in section 2.4), and fluid viscosity, μ, as follows (using primes to indicate dimensionless variables):

$$r = a(A' + y'), \quad n = a\delta n', \quad (v^r, v^\beta, v^n) = (\delta U v', U u', \delta^2 U w'), \quad p = \frac{\mu U}{a\delta} p'. \quad (2.2)$$

We also define $n' = h'(y')$ to be the free surface. At this point it is helpful to define some geometric parameters related to the curvature and torsion of the channel centreline. The curvature of the projection of the channel centreline onto a horizontal plane is given by $\epsilon = a/A = 1/A'$, the dimensionless pitch is $P' = P/a$, and the slope of the centreline of the channel is $\lambda = P'/A'$. Figure 3 shows channels with different combinations of ϵ and λ to help visualise different channel shapes.

The torsion, τ, and curvature, κ, of the helical channel at position y' across the channel

are given by

$$\tau(y') = \frac{\epsilon\Lambda(y')}{\Upsilon(y')(1+\epsilon y')}, \quad \kappa(y') = \frac{\epsilon}{\Upsilon(y')(1+\epsilon y')} = \frac{\tau(y')}{\Lambda(y')}, \tag{2.3}$$

where

$$\Lambda(y') = \frac{\lambda}{1+\epsilon y'}, \tag{2.4}$$

is the slope of the channel bottom at a point y', and for notational convenience we have introduced

$$\Upsilon(y') = 1 + \Lambda^2(y'). \tag{2.5}$$

At leading order in δ, the Navier–Stokes and continuity equations are (dropping primes):

$$-\frac{\partial p}{\partial y} + \frac{\partial^2 v}{\partial n^2} + 2\tau(y)\frac{\partial u}{\partial n} + Re\,\kappa(y)u^2 = 0, \tag{2.6a}$$

$$\frac{\partial^2 u}{\partial n^2} - \frac{Re}{Fr^2}\frac{\tau}{\sqrt{\tau^2+\kappa^2}} = 0, \tag{2.6b}$$

$$-\frac{\partial p}{\partial n} - \frac{Re}{Fr^2}\frac{\kappa}{\sqrt{\tau^2+\kappa^2}} = 0, \tag{2.6c}$$

$$\frac{\partial v}{\partial y} + \frac{\epsilon v}{1+\epsilon y} + \frac{\partial w}{\partial n} = 0, \tag{2.6d}$$

where

$$Re = \frac{\rho\delta U a}{\mu} \quad \text{and} \quad Fr = \frac{U}{\sqrt{ga\delta}} \tag{2.7}$$

are the Reynolds and Froude numbers respectively (note that the centrifugal term in (2.6*a*) could be written in terms of the Dean number $K = 2\epsilon Re^2$, as in Stokes *et al.* (2013)). The boundary conditions are no-slip on the channel bottom, *i.e.*,

$$u = v = w = 0 \quad \text{on} \quad n = 0 \tag{2.8}$$

and, on the free surface, no stress, which implies

$$p = 0, \ \frac{\partial u}{\partial n} = 0, \ \frac{\partial v}{\partial n} = 0 \quad \text{on} \quad n = h(y), \tag{2.9}$$

plus the standard kinematic condition, which gives

$$v\frac{\mathrm{d}h}{\mathrm{d}y} = w \quad \text{on} \quad n = h(y). \tag{2.10}$$

Physically, there will also be no-slip on the channel side walls ($y = \pm 1$) but we cannot impose this condition on our solutions owing to the thin-film scaling. In practice, we anticipate the presence of thin boundary layers close to these walls.

2.3. *Solution*

Expressions for the pressure, p, axial velocity component, u, and radial velocity component, v, are obtained by integrating (2.6*a*)–(2.6*c*). We obtain:

$$p = -\frac{Re}{Fr^2}\frac{\kappa}{\sqrt{\tau^2+\kappa^2}}\,(n-h)\,, \tag{2.11}$$

$$u = \frac{Re}{2Fr^2}\frac{\tau}{\sqrt{\tau^2+\kappa^2}}n\,(n-2h)\,, \tag{2.12}$$

$$v = \frac{Re}{2Fr^2}\frac{\kappa}{\sqrt{\tau^2+\kappa^2}}\frac{\mathrm{d}h}{\mathrm{d}y}n(n-2h) - \frac{Re}{2Fr^2}\frac{\tau^2}{\sqrt{\tau^2+\kappa^2}}\left\{(n-h)^3+h^3\right\}$$
$$-\frac{Re^3}{60Fr^4}\frac{\tau^2\kappa}{\tau^2+\kappa^2}n(n-2h)\left\{n^3(n-4h)+2h^2(n^2+2hn+4h^2)\right\}. \quad (2.13)$$

The continuity equation (2.6d) can be written

$$\frac{\partial}{\partial y}\Big([1+\epsilon y]v\Big) + \frac{\partial}{\partial n}\Big([1+\epsilon y]w\Big) = 0, \quad (2.14)$$

and an equation for the free-surface profile, $h(y)$, is found using the integrated form of (2.14),

$$\int_0^{h(y)} v\,\mathrm{d}n = 0 \quad (2.15)$$

which is obtained by requiring that there is no net flux into or out of the flow domain. Substituting (2.13) into (2.15) and integrating yields the differential equation for $h(y)$,

$$\frac{\mathrm{d}h}{\mathrm{d}y} = \frac{6}{35}\frac{Re^2}{Fr^2}\frac{\tau^2}{\sqrt{\tau^2+\kappa^2}}h^4 - \frac{9}{8}\frac{\tau^2}{\kappa}h, \quad (2.16)$$

which can be used to eliminate the derivative term in (2.13).

To calculate the normal velocity component, w, we use a streamfunction to describe flow in the channel cross-section. The streamfunction $\psi(y,n)$ is defined by

$$\frac{\partial\psi}{\partial n} = (1+\epsilon y)v, \quad (2.17a)$$
$$\frac{\partial\psi}{\partial y} = -(1+\epsilon y)w, \quad (2.17b)$$

and can be found by substituting v into (2.17a) and integrating subject to $\psi = 0$ on $n = h(y)$, to give

$$\psi = \frac{\epsilon Re^3}{840Fr^4}\frac{\tau\kappa}{\tau^2+\kappa^2}n^2(n-h)(n-2h)^2(2nh-n^2+4h^2)$$
$$-\frac{\epsilon Re}{16Fr^2}\frac{\tau^2\kappa}{(\tau^2+\kappa^2)^{3/2}}n^2(n-h)(2n-3h). \quad (2.18)$$

We note that ψ vanishes on the channel bottom, $n = 0$, as well as the free surface, $n = h$, as indeed it must.

We rewrite the free-surface equation (2.16) as

$$\frac{\mathrm{d}h}{\mathrm{d}y} = \frac{6}{35}\frac{Re^2}{Fr^2}\frac{\epsilon\Lambda^2}{\Upsilon^{3/2}}\frac{h^4}{(1+\epsilon y)} - \frac{9}{8}\frac{\epsilon\Lambda^2}{(1+\epsilon y)\Upsilon}h \quad (2.19)$$

and seek a solution with boundary condition $h(1) = h_r$, where h_r is the fluid depth at the outside wall of the channel. Since it is a Bernoulli differential equation, we use the substitution

$$\xi(y) = h(y)^{-3}, \quad (2.20)$$

which transforms (2.19) into the linear first-order differential equation

$$\frac{\mathrm{d}\xi}{\mathrm{d}y} - \frac{27}{8}\frac{\epsilon\Lambda^2}{(1+\epsilon y)\Upsilon}\xi = -3\frac{Re^2}{Fr^2}\frac{\epsilon\Lambda^2}{(1+\epsilon y)\Upsilon^{3/2}}, \quad (2.21)$$

which may be solved using the integrating factor $\Upsilon^{27/16}$ to give

$$h(y) = \Upsilon(y)^{9/16}\left\{\Upsilon(1)^{27/16}h_r^{-3} - \frac{144}{665}\frac{Re^2}{Fr^2}\left(\Upsilon(1)^{19/16} - \Upsilon(y)^{19/16}\right)\right\}^{-1/3}. \tag{2.22}$$

Although in the above we have imposed a boundary condition in terms of the fluid depth at the outside wall of the channel, in practice this is difficult to control, and a more natural condition to specify is the fluid flux down the channel. Thus, for a prescribed flux, we determine the corresponding value of h_r to give the appropriate free-surface profile. The dimensional flux down the channel, denoted Q, is given by

$$Q = -Ua^2\delta\int_{-1}^{1}\int_{0}^{h} u\,\mathrm{d}n\,\mathrm{d}y = Ua^2\delta\hat{Q} \tag{2.23}$$

and, on substituting for u and integrating, we find the dimensionless fluid flux

$$\hat{Q} = \frac{1}{3}\frac{Re}{Fr^2}\int_{-1}^{1}\frac{\tau}{\sqrt{\tau^2+\kappa^2}}h^3\,\mathrm{d}y. \tag{2.24}$$

Note that the minus sign appears in (2.23) because our axial coordinate direction, $\boldsymbol{e}_\beta$, points up the channel, and hence fluid flowing down the channel has negative axial velocity. In general, we cannot solve (2.24) exactly, and so cannot obtain the exact value of h_r for a chosen value, $\hat{\mathcal{Q}}$, of the flux. We solve numerically using an adaptive Gauss-Kronrod quadrature algorithm provided by Matlab to approximate the integral, and a bisection-type search method to find an approximate value of h_r such that $\hat{Q}$ is within some specified tolerance of $\hat{\mathcal{Q}}$. We have required the relative error in $\hat{Q}$ to be less than 10^{-8}. Note that we can use the fluid depth at any location in the channel as the boundary condition for (2.19), but choose $y = 1$ to improve the numerical conditioning of the search algorithm. At $y = 1$ the fluid depth is most sensitive to flux, whereas at $y = -1$ it is, in general, least sensitive, and so small changes in the depth at $y = -1$ cause very large changes in the flux, which makes calculating the appropriate boundary condition there more difficult than at $y = 1$.

The dimensional cross-sectional area of the fluid domain is denoted Ω, and is defined as

$$\Omega = a^2\delta\int_{-1}^{1} h\,\mathrm{d}y = a^2\delta\,\hat{\Omega} \tag{2.25}$$

where $\hat{\Omega}$ is the dimensionless cross-sectional area

$$\hat{\Omega} = \int_{-1}^{1} h\,\mathrm{d}y. \tag{2.26}$$

As with (2.24), we cannot in general solve this integral exactly, and must use numerical integration.

2.4. *Scaling*

Thus far, we have not specified the velocity scale, U, and depth scale, δ, in our problem. We note that the gravitational forcing term in (2.6*b*) may be written

$$\frac{Re}{Fr^2}\frac{\Lambda}{\sqrt{1+\Lambda^2}} \tag{2.27}$$

and hence we choose to set

$$\frac{Re}{Fr^2}\frac{\lambda}{\sqrt{1+\lambda^2}} = 1 \tag{2.28}$$

so that the term has unit value at the channel centreline $y = 0$. In addition, to ensure non-trivial free-surface profiles for any choice of ϵ and λ, we set the coefficient of h^4 in (2.19) to have unit value at $y = 0$, so that

$$\frac{6}{35} Re \frac{\epsilon\lambda}{1+\lambda^2} = 1. \tag{2.29}$$

With these scalings, the velocity scale is

$$U = \left[\left(\frac{35}{6\epsilon} \right)^2 \frac{(1+\lambda^2)^{3/2}}{\lambda\epsilon^2} \frac{g\mu}{\rho} \right]^{1/3} \tag{2.30}$$

and the thin-film parameter is

$$\delta = \frac{1}{a} \left[\frac{35}{6} \frac{(1+\lambda^2)^{3/2}}{\epsilon\lambda^2} \frac{\mu^2}{g\rho^2} \right]^{1/3}. \tag{2.31}$$

Note that our thin-film assumption requires $\delta \ll 1$, and this limits the possible values of the parameters. For example, for a 1m wide channel ($a = 1/2$m), with water ($\mu = 10^{-3}\,\mathrm{kg\,m^{-1}\,s^{-1}}$, $\rho = 10^3\,\mathrm{kg\,m^{-3}}$) and $g = 9.81\,\mathrm{m\,s^{-2}}$, we require

$$\frac{\epsilon\lambda^2}{(1+\lambda^2)^{3/2}} \gg 5 \times 10^{-12} \tag{2.32}$$

to ensure that δ remains small. This inequality fails to hold in only a very small part of the parameter space, when the channel approaches a straight ($\epsilon \to 0$), flat ($\lambda \to 0$), or steep (very large λ) geometry, which are not of interest here.

With this scaling, our free-surface equation (2.22) becomes

$$h(y) = \Upsilon(y)^{9/16} \left\{ \Upsilon(1)^{27/16} h_r^{-3} - \frac{24}{19} \frac{(1+\lambda^2)^{3/2}}{\epsilon\lambda^2} \left(\Upsilon(1)^{19/16} - \Upsilon(y)^{19/16} \right) \right\}^{-1/3}. \tag{2.33}$$

3. Results

We now use our analytic solution to investigate the effects of ϵ, λ, and $\hat{Q}$ on the free-surface profile, and the pressure and velocity fields. In section 3.1 we consider the free-surface profile from which we determine the fluid velocity components and pressure. In section 3.2 we present several velocity and pressure solutions, and discuss general features of the results. We give particular attention to large flux in section 3.3.

3.1. *Free-surface profile*

Figures 4 and 5 show some representative free-surface profiles for different choices of λ and ϵ at a fixed flux $\hat{Q} = 1$. These illustrate some of the qualitatively different types of free-surface profile that are possible with different channel geometry parameters ϵ and λ. For sufficiently small slope the fluid depth at the inside (left) wall of the channel, $h_l = h(-1)$, decreases with increasing curvature ϵ and the fluid depth increases monotonically across the width of the channel from the inside to the outside wall; figure 4a. For any ϵ, h_l increases with λ (figure 5), and for ϵ not too close to unity, the fluid depth increases monotonically across the width of the channel from inside to outside wall; figures 4a, 5a. However, for ϵ sufficiently close to unity and sufficiently large λ, the free surface profile changes significantly, with the fluid depth at first decreasing with distance from the inside wall and then increasing; figures 4b,c, 5b,c; there is a build-up of fluid near the inside

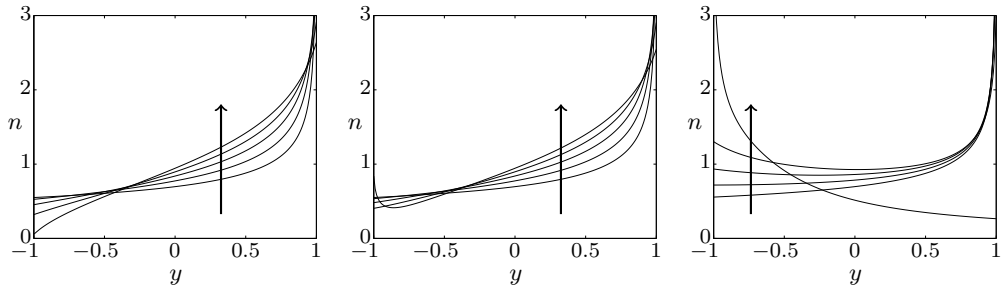

(a) $\lambda = 0.01$ (b) $\lambda = 0.2$ (c) $\lambda = 5$

Figure 4: Free-surface profiles for fixed slope λ, for curvatures $\epsilon = 0.01$, 0.255, 0.5, 0.745, 0.99, and flux $\hat{Q} = 1$. Arrows show direction of increasing ϵ.

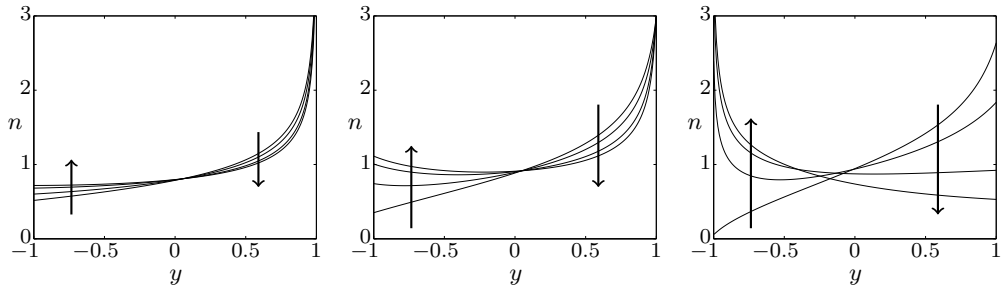

(a) $\epsilon = 0.3$ (b) $\epsilon = 0.7$ (c) $\epsilon = 0.99$

Figure 5: Free-surface profiles for fixed curvature ϵ, with slopes $\lambda = 0.01$, 0.67, 1.34, 2, and flux $\hat{Q} = 1$. Arrows show direction of increasing λ.

wall where the channel slope is largest. For very large λ and ϵ very close to unity the fluid depth is largest at the inside wall (where the channel bottom will be near vertical) and decreases monotonically across the width of the channel, figures 4c, 5c.

For small ϵ, we observe that the solutions become nearly independent of λ (figure 5a), and, indeed, this is seen from the small ϵ limit of (2.33) which is independent of λ:

$$h(y) = \left[h_r^{-3} - 3(y-1)\right]^{-1/3}. \tag{3.1}$$

Note that in this limit, exact expressions can be obtained for the flux, $\hat{Q}$, and area, $\hat{\Omega}$; see Stokes *et al.* (2013) for details. As ϵ increases to near unity, the free surface solution becomes more sensitive to changes in λ. This is intuitive — at large ϵ the slope of the channel changes significantly across its width, and so the effects of changing λ will be greater.

Increasing flux (with fixed ϵ and λ) always increases the fluid depth at any point in the channel, and the fluid depth at the outer wall, h_r, grows without bound as flux becomes infinite; see figure 6. Increasing flux tends to increase h_r more than h_l, *i.e.*, the depth at the outside wall is much more sensitive to changes in flux.

We can explain the free-surface profiles that we observe physically, in terms of two competing mechanisms, corresponding to the two terms on the right of the free-surface equation (2.19). Centrifugal force pushes the fluid to the outside wall of the channel, which is exacerbated by increasing the flux. This effect was also described by Stokes

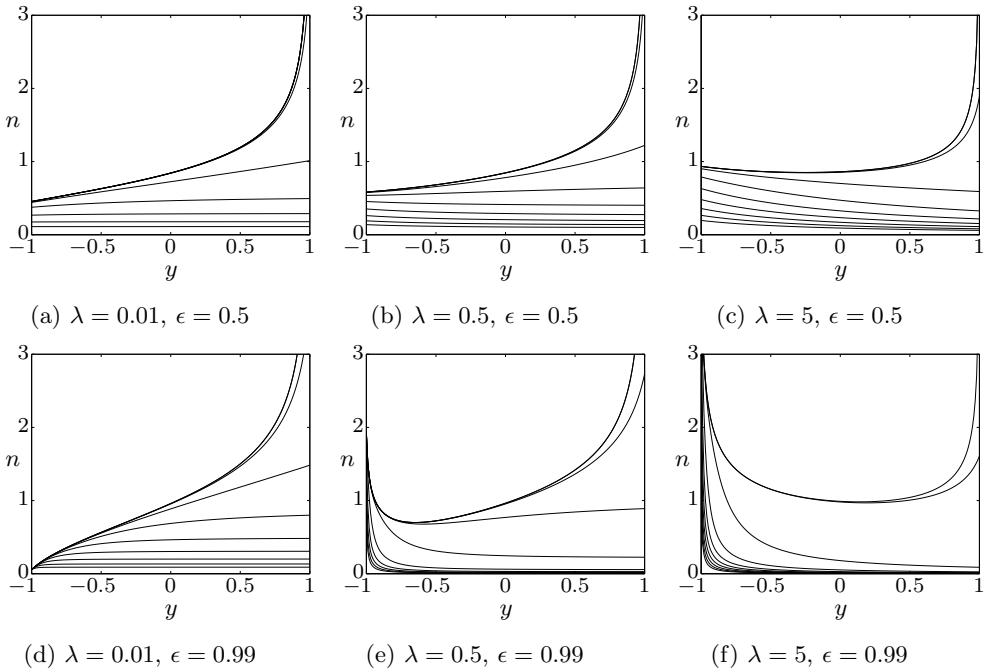

(a) $\lambda = 0.01$, $\epsilon = 0.5$ (b) $\lambda = 0.5$, $\epsilon = 0.5$ (c) $\lambda = 5$, $\epsilon = 0.5$

(d) $\lambda = 0.01$, $\epsilon = 0.99$ (e) $\lambda = 0.5$, $\epsilon = 0.99$ (f) $\lambda = 5$, $\epsilon = 0.99$

Figure 6: Free-surface profile for fixed slope λ and curvature ϵ, with varying flux $\hat{Q}$ ranging from 10^{-3} to the maximum that is computationally possible. From left to right, λ is increasing, and from top to bottom, ϵ is increasing. Increasing flux always increases fluid depth everywhere. Figure 6a is representative of plots for all λ with $\epsilon \ll 1$.

et al. (2013), and is related to the first term on the right of our free-surface equation. However the model presented in the current work also includes the effect of the varying slope across the width of the channel (neglected by Stokes *et al.* (2013) who assumed constant slope). When ϵ is close to unity, and the channel is tightly wound about the vertical axis, the channels slopes much more steeply near the inside wall than at the outside wall. This means the axial flow direction in this region is more aligned with the direction of gravitational acceleration, which results in a significant gravitational effect, captured by the second term on the right of (2.19), so that the fluid effectively cascades down the inside of the channel. This gravitational effect is magnified by increasing the slope of the channel centreline, λ. Thus there is a balance between centrifugal effects pushing the fluid to the outer wall, and gravitational effects pulling the fluid downwards and to the steepest part of the channel.

3.2. *Velocity and pressure profiles*

A representative solution for velocity components and pressure is shown in figure 7. The parameters used in this figure are chosen for a channel with curvature and slope that roughly correspond to a Vickers FGL commercial spiral separator ($\epsilon = 0.67$, $\lambda = 0.33$, Holtham 1992). Streamlines of the secondary flow and contours of the axial velocity and pressure are shown. The secondary flow shows a single rotating cell, cut off by the outer wall. The streamfunction of the secondary flow, ψ, is zero on the free-surface and channel bottom, corresponding to the top and bottom of the fluid domain, however multiple streamlines meet the channel walls, violating the no-slip condition. As explained earlier, this is due to the thin-film scaling. Boundary layers will exist which are not captured

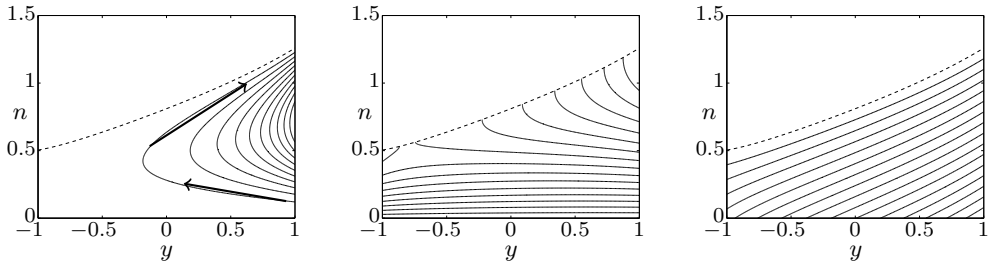

(a) Streamfunction, ψ (b) Axial velocity, u (c) Pressure, p

Figure 7: Streamlines of the secondary flow and contour plots of axial velocity and pressure, for $\lambda = 0.33$, $\epsilon = 0.67$ and for $\hat{Q} = 0.4$. Arrows indicate the direction of the secondary flow in (a).

by our leading order (in δ) equations. Stokes *et al.* (2013) compared numerical solutions to the full Navier-Stokes equations with their thin-film results, and found agreement everywhere away from the edges of the channel. Imposing no-slip on the side walls of the channel would cause streamlines to form closed curves, and we would observe a single clockwise-rotating closed cell in the channel cross-section.

In figure 7b, the axial velocity increases as the distance from the channel bottom increases, and the maximum axial velocity occurs at the outside wall of the channel on the free surface. For some choices of the geometry, notably as the slope increases significantly towards the inside wall, the maximum axial velocity u can move to the inside wall (figure 8), or somewhere between the two walls (figure 9), although it always occurs on the free-surface, $n = h(y)$ (the minimum axial velocity is, of course, zero, on the channel bottom). For any choice of parameters, at the free surface we always have a radial velocity $v > 0$ across the whole width of the channel, so we always have transport to the outside of the channel along the free surface. At the channel bottom, we always have $v = 0$, but $\partial v/\partial n < 0$ so that there we have transport to the inside wall of the channel. Nevertheless, although a single rotating cell (as in figure 7a) is the most prevalent type of cross-sectional flow, the formation of multiple rotating cells is possible. Figure 8a shows a case for large λ with two clockwise rotating cells, one close to each wall, within the outer clockwise rotating flow. This change in the flow pattern has potentially important implications for particle segregation. Segregation requires particles of different size/density to collect in different regions of the channel cross section and a secondary flow with multiple rotating cells may inhibit or facilitate particle segregation. A question still under investigation is whether more than two rotating cells can form. In visualising a large number of cross-sectional flow profiles we have seen no evidence of more than two cells, nor does our intuition suggest a mechanism by which they could form. However, we cannot, as yet, prove this claim.

The case of small slope and flux is also of interest. As shown in figure 9 we observe a free-surface with negative second derivative, and the maximum axial velocity occurs away from the channel walls (we note that this is the only case consistent with a free vortex primary flow approximation as assumed by Holland-Batt (1989, 2009)). As flux increases, centrifugal force acts to push the fluid towards the outside wall, reversing the sign of the second derivative of the free-surface profile in the vicinity of that wall.

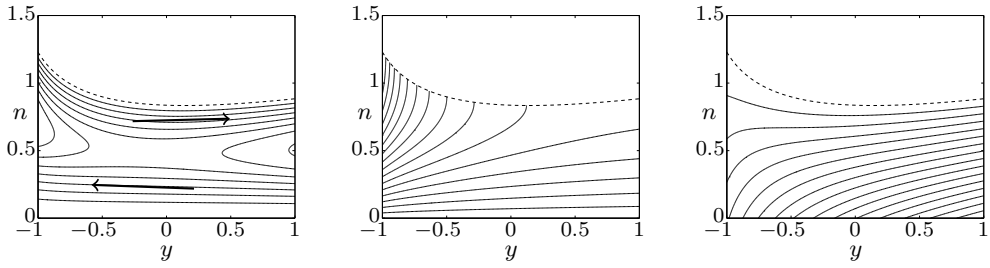

(a) Streamfunction, ψ (b) Axial velocity, u (c) Pressure, p

Figure 8: Streamlines of the secondary flow and contour plots of axial velocity and pressure, for $\lambda = 1.5$, $\epsilon = 0.8$ and for $\hat{Q} = 0.5$. Arrows indicate the direction of the secondary flow in (a).

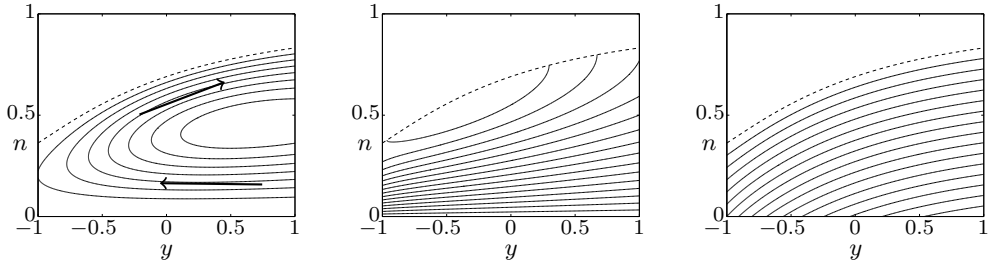

(a) Streamfunction, ψ (b) Axial velocity, u (c) Pressure, p

Figure 9: Streamlines of the secondary flow and contour plots of axial velocity and pressure, for $\lambda = 0.15$, $\epsilon = 0.75$ and for $\hat{Q} = 0.2$. Arrows indicate the direction of the secondary flow in (a).

3.3. *Large fluid flux*

In Stokes *et al.* (2013) it was found that as $\hat{Q} \to \infty$, h_l, the fluid depth at the inside wall of the channel, and $\hat{\Omega}$, the fluid cross-sectional area, each approached finite limiting values, whilst h_r, the fluid depth at the outside wall, became unbounded. We now examine if this remains true for the more general problem considered in the current paper.

Although the flux and area integrals, (2.24) and (2.26), cannot be evaluated in closed form, elementary manipulations of the free-surface equation (2.19), allow us to express the cross-sectional area as

$$\hat{\Omega} = \frac{1}{2h_l^2}\left(\frac{\lambda^2+(1-\epsilon)^2}{\lambda^2+1}\right)^{3/2} + \frac{1}{2}\frac{\epsilon\lambda^2}{(1+\lambda^2)^{3/2}}\int_{-1}^{1}\frac{9}{4}\frac{\sqrt{\Upsilon}}{h^2} + 3\frac{\sqrt{\Upsilon}}{\Lambda^2}\frac{1}{h^2}\,\mathrm{d}y - \frac{1}{2h_r^2}\left(\frac{\lambda^2+(1+\epsilon)^2}{\lambda^2+1}\right)^{3/2}, \tag{3.2}$$

and the flux as

$$\hat{Q} = \frac{3}{8}\frac{\lambda^2}{1+\lambda^2}\log\left(\frac{1+\epsilon}{1-\epsilon}\right) - \frac{1}{3}\frac{\lambda^2+(1-\epsilon)^2}{1+\lambda^2}\log(h_l) - \frac{2}{3}\frac{\epsilon}{1+\lambda^2}\int_{-1}^{1}(1+\epsilon y)\log(h(y))\,\mathrm{d}y + \frac{1}{3}\frac{\lambda^2+(1+\epsilon)^2}{1+\lambda^2}\log(h_r). \tag{3.3}$$

We further note that there is a maximum possible fluid depth at $y = -1$, h_{l_M}, such that $0 < h_l < h_{l_M}$ where

$$h_{l_M} = \left\{ \frac{24}{19} \frac{(1-\epsilon)(1+\lambda^2)^{3/2}}{\epsilon\lambda^2\sqrt{\lambda^2+(1-\epsilon)^2}} \left[1 - \left(\frac{(1-\epsilon^2)^2+\lambda^2(1-\epsilon)^2}{(1-\epsilon^2)^2+\lambda^2(1+\epsilon)^2} \right)^{19/16} \right] \right\}^{-1/3}, \tag{3.4}$$

which is found by considering the limit as $h_r \to \infty$ of (2.33) at $y = -1$.

We consider equations (3.2) and (3.3) in the limit $h_r \to \infty$. In (3.2), all three terms are bounded in this limit, so $\hat{\Omega}$ is bounded. In figure 10a, the complete expression for $\hat{\Omega}$ (evaluated numerically) is plotted, along with the first two terms in (3.2), showing the area reaching a limiting value (approximately 2.1 for the parameter values chosen). It can be shown that the first three terms in (3.3) are bounded as $h_r \to \infty$, and hence

$$\hat{Q} \sim \frac{1}{3} \frac{\lambda^2+(1+\epsilon)^2}{1+\lambda^2} \log(h_r) \quad \text{as } h_r \to \infty. \tag{3.5}$$

This behaviour is illustrated by figure 10b, for the case $\lambda = 0.5$, $\epsilon = 0.5$. We have thus confirmed that for large fluxes ($\hat{Q} \to \infty$), the qualitative behaviour of h_l, h_r and $\hat{\Omega}$ is the same as that found in Stokes *et al.* (2013).

The maximum fluid depth at the inner wall, h_{l_M} is plotted against ϵ for different values of λ in figure 11. For $\epsilon < 1$, h_{l_M} is bounded. In the limit $\epsilon \to 0$, (3.4) reduces to $h_{l_M} = 6^{-1/3}$, which is independent of λ. Limits of h_{l_M} as $\lambda \to 0$ and $\lambda \to \infty$ are also plotted (dashed curves). It can be seen from the plot, and confirmed by taking limits, that as $\epsilon \to 1$, $h_{l_M} \to \infty$ for any $\lambda > 0$.

Figure 12 shows the effect of increasing the flux, $\hat{Q}$, on the cross-sectional area of the flow, $\hat{\Omega}$. As shown above, and in Stokes *et al.* (2013), $\hat{\Omega}$ approaches an upper bound as $\hat{Q}$ becomes large. Roughly speaking, a flux of around two to three is sufficient for $\hat{\Omega}$ to approach its limiting value, corresponding to h_l nearing its limiting value h_{l_M}, and in the specific case $\epsilon = 0.5$ and $\lambda = 0.5$, equivalent to $h_r \approx 10$. This suggests that a flux of roughly two to three is representative of large flux. In this regime, increasing ϵ increases the cross-sectional area. However when flux is small a different relationship is observed. Figure 12b magnifies the $0 \leqslant \hat{Q} \leqslant 0.5$ region of figure 12a, showing the difference more clearly. We see that $\hat{\Omega}$ does not vary significantly until ϵ nears unity, when it decreases. Thus for small flux, cross-sectional area is weakly dependent on ϵ over much of the parameter space, but for large flux the dependence is stronger. Equivalent plots, omitted for brevity, with fixed ϵ and varying λ show little variation between curves for different values of λ, showing that cross-sectional area depends weakly on the slope of the channel bottom.

4. Conclusions

We have considered flow in helically-wound channels of rectangular cross-section, assuming the flow to be helically symmetric, and that the typical depth of the fluid is small so that a thin-film approximation is appropriate. The Navier-Stokes equations were expressed in a non-orthogonal coordinate system, then transformed to three orthogonal directions: $\boldsymbol{e}_\beta$ in the direction of increasing angle β along the helical centreline, $\boldsymbol{e}_r$ in the horizontal radial direction, and $\boldsymbol{e}_n$ normal to the bottom of the channel.

The most convenient parameters for describing the geometry of the channel were found to be ϵ, corresponding to the curvature of the circle obtained by projecting the helical centreline onto a horizontal plane, and λ, the slope of the channel centreline. Effectively, these parameters correspond to the radius A and the pitch $2\pi P$ of the centreline. We have

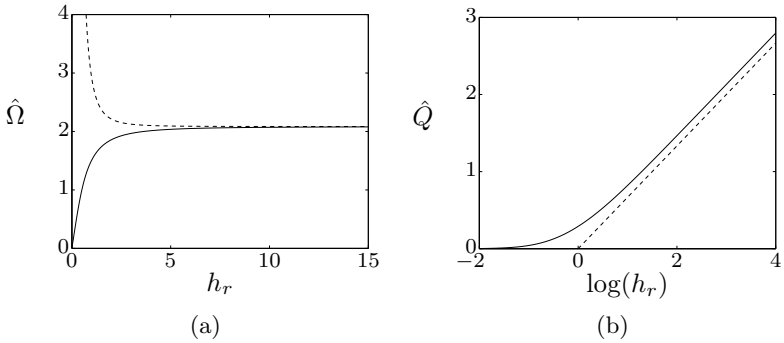

Figure 10: The dependence of (a) cross-sectional area $\hat{\Omega}$, and (b) flux $\hat{Q}$ on h_r with $\epsilon = 0.5$ and $\lambda = 0.5$. Note different x-axes. The solid curves are given by (3.2) and (3.3) respectively; the dashed curves are (a) the first two terms, and (b) the last term of these expressions.

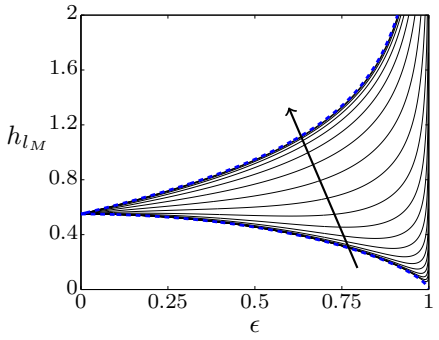

Figure 11: Maximum fluid depth at the inside wall, h_{l_M}, against ϵ. Different curves correspond to different values of λ, the arrow showing the direction of increasing λ. Dashed curves are the $\lambda \to 0$ and $\lambda \to \infty$ limits.

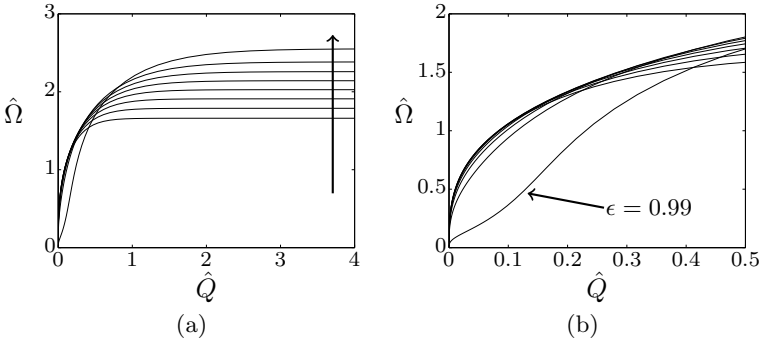

Figure 12: Fluid cross-sectional area against flux. Plotted for $\epsilon = 0.01$, 0.15, 0.29, 0.43, 0.57, 0.71, 0.85, 0.99, with $\lambda = 0.5$. The arrow in (a) shows the direction of increasing ϵ.

$\epsilon = 1/A$ and $\lambda = P/A$, and for physically meaningful channels we must have $0 < \epsilon < 1$. For a right-hand helix we take $\lambda > 0$. The commonly used curvature and torsion of the channel centreline may be expressed in terms of ϵ and λ. The general solution we obtain is valid for channels with centrelines of arbitrary curvature and torsion. The case where torsion is large at the inside wall but small at the channel centreline, corresponding to ϵ very near 1, was identified in Stokes *et al.* (2013) as requiring further investigation. In that paper, torsion and curvature were considered constant across the width of the channel, but here we account for their variation. This explains differences observed between our results and those of Stokes *et al.* (2013).

The free-surface profile is given by the solution of the ordinary differential equation (2.16). The equation has an analytic solution, (2.22). Three parameters govern our solutions: ϵ, the modified curvature, λ, the slope of the channel, and $\hat{Q}$, the dimensionless fluid flux down the channel. We use scalings to relate the Reynolds and Froude numbers to the geometric parameters ϵ and λ in order to plot results. The three parameters are all important, and their effects are complicated, but we can make general statements about their effects on the solutions, and some conclusions hold independently of geometry. We find the fluid depth at the inside wall (h_l) is bounded for all curvature $\epsilon < 1$, and the fluid depth at the outside wall becomes unbounded ($h_r \to \infty$) as $\hat{Q} \to \infty$ for any geometry. We always have transport to the outside of the channel at the free-surface, and transport to the inside of the channel near the bottom. Rotating cells always rotate clockwise. Most other conclusions, however, are dependent on geometry.

The effects of geometry and flux can be characterised by considering the balance of gravitational and centrifugal effects. The steeper the channel, the more aligned the channel bottom with the vertical direction, and hence the stronger the gravitational effects on the flow. We have steep channels for large λ, and at the inside wall when ϵ is large, and in these cases the free surface has a negative gradient at the inside wall. Centrifugal effects are dominant when the fluid flux is large, when ϵ is small, or λ is not large. They drive fluid to the outside wall of the channel which results in a free surface with positive gradient near this wall. For moderate parameter values we see these two effects competing.

For a channel with small curvature (large centreline radius), the solutions depend weakly on the slope of the centreline. We see the fluid depth increasing monotonically across the channel from inside to outside wall, a single clockwise rotating cell in the cross section, and the maximum axial velocity at the outside wall. For a channel with large curvature (small centreline radius), the solution depends strongly on the slope of the centreline and the flux, and solutions change qualitatively as these parameters vary. For example, in place of a single rotating cell in the cross section, two cells may develop, which has not been previously seen from analyses assuming small torsion or small slope.

The impact of flux and geometry on the flow solution, especially for channels with large curvature, has some practical implications. Whilst the shape of a channel (and thus λ and ϵ) would not change during operation of a spiral separator, the flux may vary, and in some regimes this would significantly affect the flow. This, in turn, might alter the particle separation capabilities of the spiral. Again we point out that our analysis does not, in general, support the approximation of the primary flow by a free vortex flow as done by Holland-Batt (1989, 2009).

Future work will investigate channels with arbitrarily shaped cross-sections, rather than the simple rectangular channels we have here considered. Spiral particle separators typically feature curved cross-sections and our equations can be generalised for such geometries. We will also extend our model to particle-laden flow in channels of arbitrary curvature and slope (torsion) by coupling to a particle transport model as in the work

of Lee *et al.* (2014) who considered monodisperse particulate flow in channels of small slope.

Acknowledgements

We gratefully acknowledge funding from an Australian Postgraduate Award to DJA, and an Australian Research Council Discovery Early Career Researcher Award (DE130100031) to JEFG. We also thank an anonymous referee for several insightful comments that have resulted in substantial improvements to this paper.

Appendix A. Orthogonal equations

The Navier-Stokes equations in the r, β, n coordinate system are presented in Lee *et al.* (2014) which can be consulted for full details. For completeness, we summarise them below. Note that whilst these equations are valid for a fluid with spatially-varying viscosity, in the current work we consider fluids of constant viscosity, so derivatives of μ vanish.

The continuity equation is

$$\frac{1}{r}\frac{\partial}{\partial r}\left(rv^r\right)+\frac{\partial v^n}{\partial n}=0 \quad \text{or} \quad \frac{\partial v^r}{\partial r}+\frac{v^r}{r}+\frac{\partial v^n}{\partial n}=0, \tag{A 1}$$

while the momentum equations are, in the $\mathbf{e}_r$ direction,

$$\begin{aligned}\rho\left[v^r v^r_{,r}+v^n v^r_{,n}-\frac{1}{r\Upsilon}\left(v^\beta-\Lambda v^n\right)^2\right] &= -p_r+\mu\left[v^r_{,rr}+v^r_{,nn}+\frac{1}{r}\left(v^r_{,r}-\frac{v^r}{r}\right)\right.\\ &\left.+\frac{2\Lambda}{r\Upsilon}\left(v^\beta_{,n}-\Lambda v^n_{,n}\right)\right]+2\mu_{,r}v^r_{,r}+\mu_{,n}\left[v^r_{,n}+v^n_{,r}-\frac{\Lambda^2}{r\Upsilon}v^n\right],\end{aligned} \tag{A 2a}$$

in the $\mathbf{e}_\beta$ direction,

$$\begin{aligned}\rho\left(v^r v^\beta_{,r}+v^n v^\beta_{,n}+\frac{1}{r\Upsilon}v^r v^\beta\right) &= \mu\left[v^\beta_{,rr}+v^\beta_{,nn}+\frac{1}{r}v^\beta_{,r}-\frac{2\Lambda}{r\Upsilon}\left(v^r_{,n}-v^n_{,r}\right)\right.\\ &\left.-\left(\frac{1+2\Lambda^2}{r^2\Upsilon^2}\right)v^\beta+\frac{2\Lambda^3}{r^2\Upsilon^2}v^n\right]+\mu_{,r}\left[v^\beta_{,r}-\frac{1}{r\Upsilon}\left(v^\beta-2\Lambda v^n\right)\right]\\ &+\mu_{,n}\left[v^\beta_{,n}-\frac{2\Lambda}{r\Upsilon}v^r\right]-\frac{\Lambda}{\sqrt{\Upsilon}}\rho g,\end{aligned} \tag{A 2b}$$

and in the $\boldsymbol{e}_n$ direction,

$$\begin{aligned}\rho\left(v^r v^n_{,r}+v^n v^n_{,n}-v^r\frac{\Lambda}{r\Upsilon}\left(2v^\beta-\Lambda v^n\right)\right) &= -p_n+\mu\left[v^n_{,rr}+v^n_{,nn}-\frac{2\Lambda}{r\Upsilon}\left(v^\beta_{,r}-\Lambda v^r_{,n}\right)\right.\\ &\left.+\frac{1}{r}\left(v^n_{,r}-\frac{v^n}{r}\right)+\frac{1}{r^2\Upsilon^2}\left(v^n+2\Lambda v^\beta\right)\right]+\mu_{,r}\left[v^r_{,n}+v^n_{,r}-\frac{\Lambda^2}{r\Upsilon}v^n\right]\\ &+2\mu_{,n}\left[\frac{\Lambda^2}{r\Upsilon}v^r+v^n_{,n}\right]-\frac{1}{\sqrt{\Upsilon}}\rho g.\end{aligned} \tag{A 2c}$$

REFERENCES

Das, S. K., Godiwakka, K. M., Panda, L., Bhattacharya, K. K., Singh, R. & Mehrotra, S. P. 2007 Mathematical modeling of separation charactersistics of a coal-washing spiral. *Int. J. Miner. Process.* **84**, 118–132.

Dean, W. R. 1927 XVI. Note on the motion of fluid in a curved pipe. *Phil. Mag.* **4** (20), 208–223.

Dean, W. R. 1928 Fluid motion in a curved channel. *Proc. R. Soc. Lond. A* **121** (787), 402–420.

Germano, M. 1982 On the effect of torsion on a helical pipe flow. *J. Fluid Mech.* **125**, 1–8.

Germano, M. 1989 The Dean equations extended to a helical pipe flow. *J. Fluid Mech.* **203**, 289–305.

Holland-Batt, A. B. 1975 A quantitative model of the motion of particles in the RSM/Mintek on-stream particle size analyser. *Powder Technol.* **11**, 11–25.

Holland-Batt, A. B. 1989 Spiral separation: theory and simulation. *Trans. Instn. Min. Metall. (Sect. C: Mineral Process. Extr. Metall.)* **98**, C46–C60.

Holland-Batt, A. B. 1995 Some design considerations for spiral separators. *Miner. Eng.* **8** (11), 1381–1395.

Holland-Batt, A. B. 2009 A method for the prediction of the primary flow on large diameter spiral troughs. *Miner. Eng.* **22** (4), 352–356.

Holland-Batt, A. B. & Holtham, P. N. 1991 Particle and fluid motion on spiral separators. *Miner. Eng.* **4** (3/4), 457–482.

Holtham, P. N. 1990 Flow visualisation of secondary currents on spiral separators. *Miner. Eng.* **3** (3/4), 279–286.

Holtham, P. N. 1992 Primary and secondary fluid velocities on spiral separators. *Miner. Eng.* **5** (1), 79–91.

Lee, S., Stokes, Y. M. & Bertozzi, A.L. 2014 Behaviour of a particle-laden flow in a spiral channel. *Phys. Fluids* **26**.

Lynch, D. G., Waters, S. L. & Pedley, T. J. 1996 Flow in a tube with non-uniform time-dependent curvature: governing equations and simple examples. *J. Fluid Mech.* **323**, 237–265.

Manoussaki, D. & Chadwick, R. S. 2000 Effects of geometry on fluid loading in a coiled cochlea. *SIAM J. Appl. Math.* **61** (2), 369–386.

Matthews, B. W., Fletcher, C. A. J. & Partiridge, A. C. 1998 Computational simulation of fluid and dilute particulate flows on spiral concentrators. *Appl. Math. Model.* **22**, 965–979.

Matthews, B. W., Fletcher, C. A. J., Partiridge, A. C. & Vasquez, S. 1999 Computations of curved free surface water flow on spiral concentrators. *J. Hydraul. Eng.* **125**, 1126–1139.

Siggers, J. H. & Waters, S. L. 2005 Steady flows in pipes with finite curvature. *Phys. Fluids* **17**.

Siggers, J. H. & Waters, S. L. 2008 Unsteady flows in pipes with finite curvature. *J. Fluid Mech.* **600**, 133–165.

Stokes, Y. M. 2001 Flow in spiral channels of small curvature and torsion. In *IUTAM symposium on free surface flows* (ed. A. C. King & Y. D. Shikhmurzaev), *Fluid mechanics and its applications*, vol. 62, pp. 289–296. Kluwer Academic Publishers.

Stokes, Y. M., Duffy, B. R., Wilson, S. K. & Tronnolone, H. 2013 Thin-film flow in helically wound rectangular channels with small torsion. *Phys. Fluids* **25** (8).

Stokes, Y. M., Wilson, S. K. & Duffy, B. R. 2004 Thin-film flow in open helically-wound channels. In *Proceedings of the 15th Australiasian fluid mechanics conference* (ed. M. Behnia, W. Lin & G. D. McBain). The University of Sydney.

Thomson, J. 1876 On the origin of windings of rivers in alluivial plains with remarks on the flow of water round bends in pipes. *Proc. R. Soc. Lond* **25** (171–178), 5–8.

Thomson, J. 1877 Experimental demonstration in respect to the origin of windings of rivers in alluvial plains, and to the mode of flow of water round bends of pipes. *Proc. R. Soc. Lond* **26** (179–184), 356–357.

Wang, J. & Andrews, J.R.G. 1994 Numerical simulations of liquid flow on spiral concentrators. *Miner. Eng.* **7** (11), 1363–1385.

Zabielski, L. & Mestel, A. J. 1998 Steady flow in a helically symmetric pipe. *J. Fluid Mech.* **370**, 297–320.